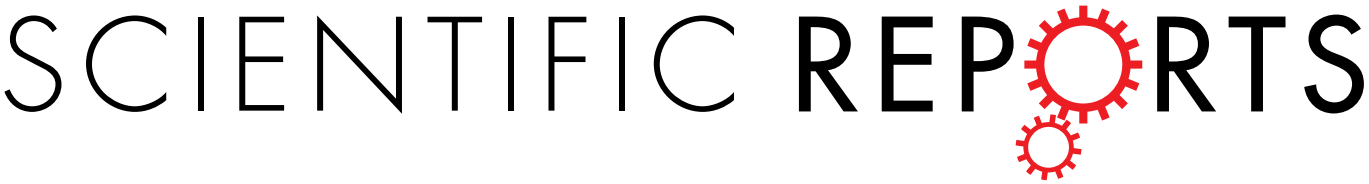

OPEN

Received: 24 March 2017
Accepted: 25 May 2017
Published online: 07 July 2017

Morphology Control of Energy-Gap-Engineered Nb_2O_5 Nanowires and the Regioselective Growth of CdS for Efficient Carrier Transfer Across an Oxide-Sulphide Nanointerface

Tomoki Shinohara, Miyu Yamada, Yuki Sato, Shohei Okuyama, Tatsuto Yui, Masayuki Yagi & Kenji Saito

Semiconductor nanowires with both nano- and micrometre dimensions have been used as effective materials for artificial photosynthesis; however, a single synthesis approach to provide rational control over the macroscopic morphology, which can allow for the high-throughput screening of photocatalytic performance, and carrier transfer between oxide and sulphide nanostructures has been poorly known. Our recent findings indicate that a single parameter, Nb foil thickness, in a vapor-phase synthesis method can alter the macroscopic morphology of resulting Nb_2O_5 nanowires. Thick Nb foil results in a free-standing Nb_2O_5 film, whereas a thinner foil leads to fragmentation to give a powder. During the synthesis process, a Rh dopant was provided through metal-organic chemical vapor deposition to reduce the Nb_2O_5 energy gap. Upon irradiation with visible light ($\lambda > 440$ nm), the free-standing nanowire film [Nb_2O_5:Rh-NW(F)] showed photoanodic current with a Faradaic efficiency of 99% for O_2 evolution. Under identical irradiation conditions, the powdered counterpart [Nb_2O_5:Rh-NW(P)] showed activity for O_2 evolution in the presence of an electron acceptor. The poor water-reduction ability was greatly enhanced by the Au-catalysed vapor-liquid-solid (VLS) growth of H_2-evolving CdS onto the reduction sites of Nb_2O_5:Rh-NW(P) [Au/CdS/Nb_2O_5:Rh-NW(P)].

Artificial photosynthesis harnessing sunlight to construct chemical bonds for use as a fuel is a key technologies to move towards a sustainable society[1–3]. Among the relevant studies, one-dimensional nanostructuring of a semiconductor photocatalyst has a great potential to accelerate the development of this technology, which has been the focus of several reports[4–6]. The unique photoresponse of nanowires results from their inherent physical properties, including very high aspect ratio and large surface area. However, the high aspect ratio imposes a limitation to the macroscopic morphology, *i.e.*, the nanowires must align at a right angle to the planar substrate for use in photoelectrocatalysis, to weaken the light scattering and to streamline carrier transfer between the nanowire and substrate. In general, synthetic routes entirely from solution for photoelectrocatalyst materials for water splitting are still limited, and previously, the syntheses of aligned nanowires as photoelectrocatalysts and non-oriented nanowires as heterogeneous photocatalysts have been rooted in well-established, vapor- and liquid-phase methods, respectively[7–14].

Niobium pentoxide with a composition formula of Nb_2O_5 is a white semiconductor material with both favourable photocatalytic performance and high chemical stability. The photocatalytic applications of Nb_2O_5, particularly regarding its visible-light response, are continuously widening. Huang, H. *et al.* reported that mesoporous, nitrogen-doped Nb_2O_5 showed an efficient visible-light performance for H_2 evolution[15]. Bonding Nb_2O_5 with another semiconductor material, such as graphitic carbon nitride (C_3N_4)[16], reduced graphene oxide[17], or cadmium sulphide (CdS)/nitrogen-doped graphene[18], opens ways to harness visible light as well. However, even

Department of Materials Science and Technology, Faculty of Engineering, Niigata University, 8050 Ikarashi-2, Niigata, 950-2181, Japan. Correspondence and requests for materials should be addressed to K.S. (email: ksaito@eng.niigata-u.ac.jp)

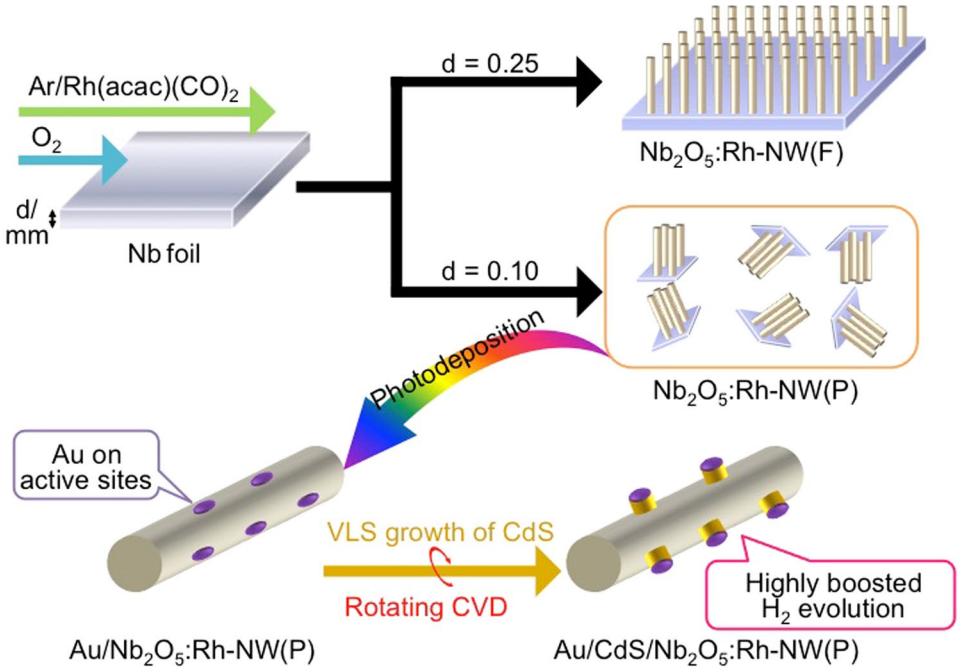

Figure 1. An overview of the morphology control and the rational 3D functionalization of the Rh-doped Nb_2O_5 nanowire.

though the valence-band maximum of Nb_2O_5 is high enough to oxidize water (ca. 3 eV vs. NHE), reports on the O_2 evolution reaction over Nb_2O_5 have been rare, regardless of the exploitable wavelength of light[19].

Contrary to a single photocatalyst, the combination of two separate photocatalysts with H_2 and O_2 evolution centres, referred to as a Z-scheme photocatalyst, liberalizes the thermodynamic restrictions on water splitting, where the water-reduction/oxidation potentials must be located between the potential energies of the conduction-band minimum and valence-band maximum of the photocatalysts[20]. Hence, many combinations have been screened and subsequently discovered[1,2]. Among them, oxide-sulphide combinations are promising candidates because oxides and sulphides possess strong oxidation and reduction capabilities, respectively[21–31]. Ideally, an H_2-evolving sulphide should be placed on the reduction site of the oxide because this positional relationship allows for efficient carrier transfer, and excessive sulphide utilization or deposition on the oxide could provoke a light-shielding effect. However, such a strategy is poorly understood.

A vapor-liquid-solid (VLS) mechanism is an established technology that allows for controlled growth of nanostructured material by a metal catalyst with control of the location, size, etc.[32,33]. Of course, this technology can be applied to metal-sulphide deposition onto an oxide photocatalyst to construct a Z-scheme photocatalyst. However, the extremely low permeability of the vapor source into the solid hampers the application of the VLS mechanism to powdered photocatalysts. On the other hand, photodeposition is a well-known technique in which a metal cocatalyst is formed on the reduction site of the photocatalyst[19]. Therefore, a combination of VLS and photodeposition could pave a new path to construct oxide-sulphide composite photocatalysts if the permeability problem is solved adequately.

Here, we report a single synthesis approach of band-gap-engineered Nb_2O_5 nanowires with two different macroscopic morphologies, namely, a free-standing film and a powdered form. In addition, the physical rotation[34], used in the VLS growth of CdS on the reduction site of the nanowire powder, was found to have an obvious effect on the H_2 evolution activity (Fig. 1).

Results and Discussion

Structure characterization and physical properties. Figure 2 shows the FE-SEM images of the nanowires synthesized from Nb foil with two different thicknesses, Nb_2O_5:Rh-NW(F) and Nb_2O_5:Rh-NW(P). Nb_2O_5:Rh-NW(F) forms nearly-vertical, free-standing nanowires with diameters ranging from 30 to 140 nm (Fig. 2a and b). Since the diameter dimension is similar to that of the undoped counterpart film [Nb_2O_5-NW(F), Figure S1], $Rh(acac)(CO)_2$, which was constantly provided as a Rh dopant during the Nb_2O_5 synthesis, does not have a visual impact on the product morphology. The nanowires observed in Nb_2O_5:Rh-NW(P) possess similar diameters but are linked to the cornerstones with sizes of several μm (Fig. 2c and d).

The diffraction pattern of Nb_2O_5:Rh-NW(P) corresponds to the structure of *monoclinic* Nb_2O_5 (PDF 37-1468, Figure S2). XRD also indicates no existence of Rh_2O_3 that is envisioned to form by oxidative thermal decomposition of $Rh(acac)(CO)_2$, suggesting one of two possibilities: a lack or a doping of Rh in the lattice. In principle, the latter should be accompanied by a peak shift depending on the magnitude of the doping metal ions incorporated into the lattice, as formulated by Bragg. In this case, however, the ionic radius of six-coordinated Nb^{5+} is between those of Rh^{3+} and Rh^{4+}, both of which can stably exist in the metal oxide [ionic radii (Å); Nb^{5+}:0.64, Rh^{3+}:0.665,

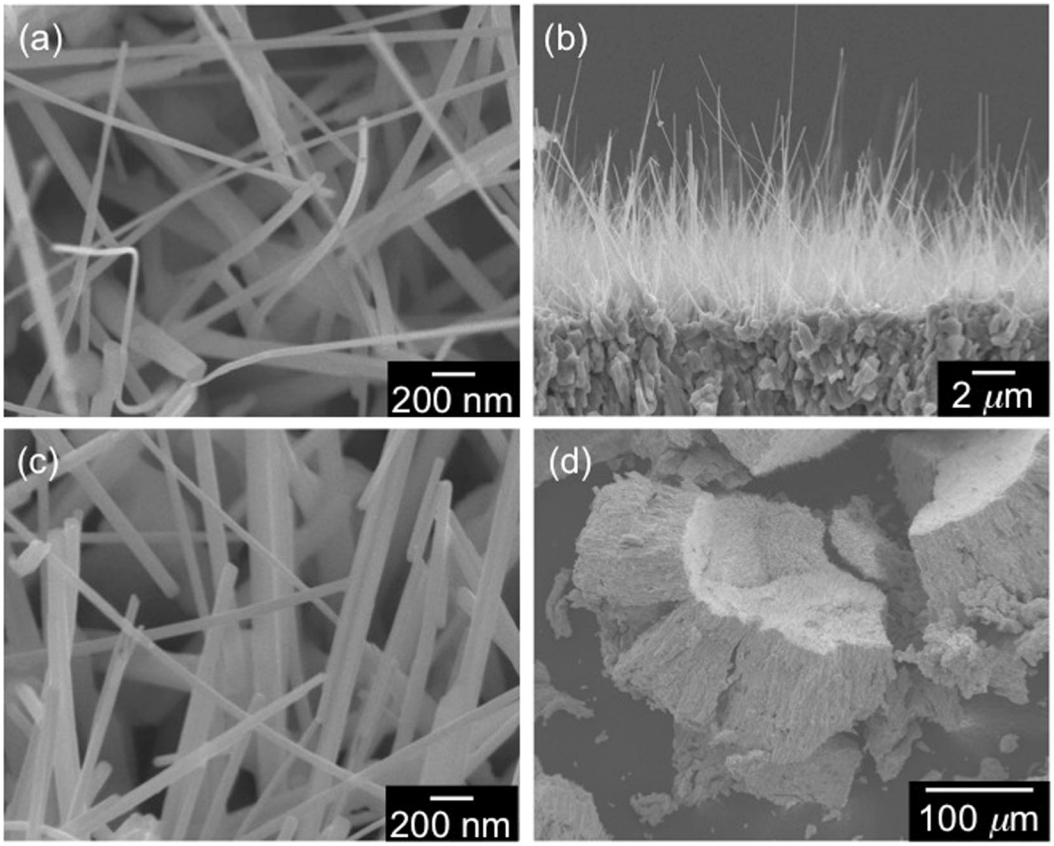

Figure 2. FE-SEM images of (**a**,**b**) Nb_2O_5:Rh-NW(F) and (**c**,**d**) Nb_2O_5:Rh-NW(P). (**a** and **c**) are the magnified views of (**b** and **d**), respectively.

Rh^{4+}:0.6). This means that, if Rh as a dopant possesses a mixed-valence state, it is hard to predict whether a peak shift, based on Bragg's law, will occur.

The XPS spectrum of Nb_2O_5:Rh-NW(P) shows the clear presence of Rh; however, it was not easy to determine whether Rh introduced in the oxide nanowire possesses trivalent and/or tetravalent states, due to the small inter-peak distance (~0.3 eV, Figure S3)[35]. The molar ratio of Rh to Nb, determined from the spectral deconvolution, was 0.13.

Nb_2O_5:Rh-NW(P) shows distinct visible absorption that is absent in the corresponding undoped counterpart, Nb_2O_5-NW(P) (Fig. 3). The emergent spectral shape largely differs from that of the Nb_2O_5/Rh_2O_3 mixture (Figure S4), whereas there was shown to be no major difference in those of Rh-doped TiO_2 and $SrTiO_3$[36,37]. Nb_2O_5:Rh-NW(P) was then reduced by H_2 to confirm the oxidation state of Rh. The absorptions at approximately 427 nm increases with the H_2 reduction treatment, while the feature at 600 nm decreases. These observed phenomena are similar to those of $SrTiO_3$:Rh with both Rh^{3+} and Rh^{4+}, and hence, we conclude that the optical transitions in the visible region result from the coexistence of Rh^{3+} and Rh^{4+} in Nb_2O_5. Therefore, Rh doping led to no peak shift in the XRD pattern of Nb_2O_5 (Figure S2). The inset of Fig. 3 shows a predicted energy diagram of Nb_2O_5:Rh-NW, which is constructed based on earlier studies[36,37]. The energy-gap values for Nb_2O_5:Rh-NW are as follows: the energy gaps between the valence-band maximum, formed mainly from O 2p orbitals, and the Rh^{4+} impurity level is 2.1 eV and between the Rh^{3+} impurity level and the conduction-band minimum, formed mainly from Nb 4d orbitals, is 2.5 eV.

Plausible growth mechanism. The non-doped Nb_2O_5-NW(F) is proposed to grow through a self-catalytic growth mechanism[38]. The nanoparticles derived from $Rh(acac)(CO)_2$, observed in the initial stages of the nanowire growth, are the last to disappear. This indicates that a successive supply of Rh does not hinder the nanowire growth and makes the penetration of Rh to the Nb_2O_5 crystal lattice easier. On the other hand, cornerstones sustaining nanowire bundles are found in Nb_2O_5:Rh-NW(P) (Fig. 2d). This observation results from a segregation phenomenon accompanied by the complete disappearance of metallic Nb, resulting in the remaining planar Nb_2O_5 substrate becoming more brittle than the substrate with the metallic Nb backbone.

Photocatalytic performance. The photoelectrochemical performances of Nb_2O_5:Rh-NW(F) and Nb_2O_5-NW(F) as a reference were examined under visible-light irradiation ($\lambda > 440$ nm). For the linear sweep voltammograms shown in Fig. 4, Nb_2O_5:Rh-NW(F) showed a well-marked, higher anodic current at potentials greater than 0.2 V (vs. SSCE) than Nb_2O_5-NW(F). The Faradaic efficiency at 0.45 V for the Nb_2O_5:Rh-NW(F)

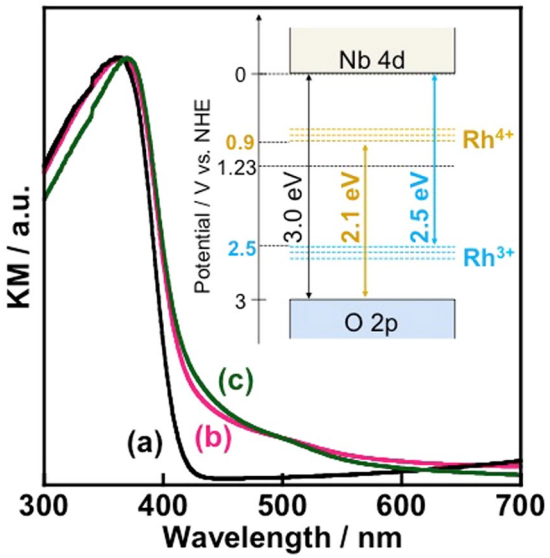

Figure 3. DRS of (**a**) Nb_2O_5-NW(P), (**b**) Nb_2O_5:Rh-NW(P), and (**c**) Nb_2O_5:Rh-NW(P) that was subjected to H_2 at 673 K, followed by calcination at 1073 K in air. The latter process was carried out because the Rh dopant and the Nb host are reduced by the H_2 treatment, resulting in a large increase in absorption due presumably to low-valent Nb, particularly at wavelengths longer than 500 nm. The energy gaps are calculated from the intersection of the tangential line from the given absorption and baseline. The inset shows the band structure constructed from the DRS results.

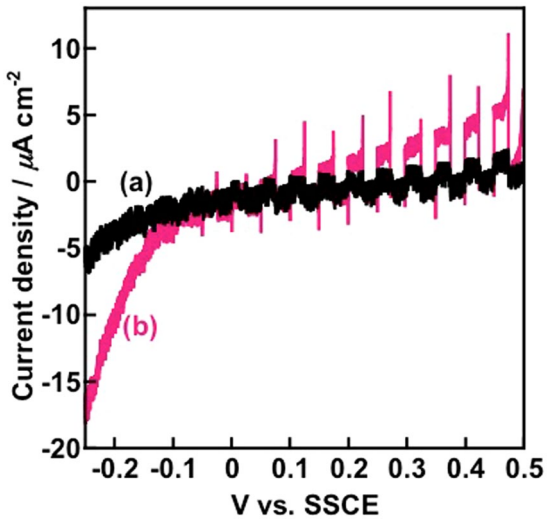

Figure 4. Current density vs. voltage characteristics of (**a**) Nb_2O_5-NW(F) and (**b**) Nb_2O_5:Rh-NW(F) taken with a sweep rate of 10 mV min^{-1} under irradiation of visible light from a 100-W Xe lamp with a Y44 cutoff filter. A 0.1 M phosphate buffer solution was used as an electrolyte.

photoanode was estimated to be 99%, indicating that the observed photocurrent results from O_2 evolution (Figure S5). On the other hand, the Y-44 filter used in the experiments does not possess light transmittance below 430 nm. Nb_2O_5-NW(F) showed an imperceptible photoresponse, which could represent an oxygen vacancy-induced photoresponse[39] due to the poor oxygen supply in our vacuum-processing system during Nb_2O_5 growth. In fact, Nb_2O_5-NW is tinged pale blue, which may also suggest a gradual increase in absorption at longer wavelengths (Fig. 3a).

Using the powdered counterpart, we examined the heterogeneous photocatalysis under identical irradiation conditions. Similar to the photoelectrochemical results, Nb_2O_5:Rh-NW(P) was found to oxidize water in the presence of an electron acceptor, Ag^+, showing much higher activity than Nb_2O_5-NW(P) (Fig. 5a). In light of the energy structure, the observed oxygen evolution should be driven by the electronic transition from Rh^{3+} to the conduction band of the Nb_2O_5 host because electron transfer from the Rh^{4+} impurity level (supplied from the valence band of Nb_2O_5) to Ag^+ is an endergonic process ($Ag^+ + e^- \rightarrow Ag$: $E^0 = 0.8$ V vs. NHE).

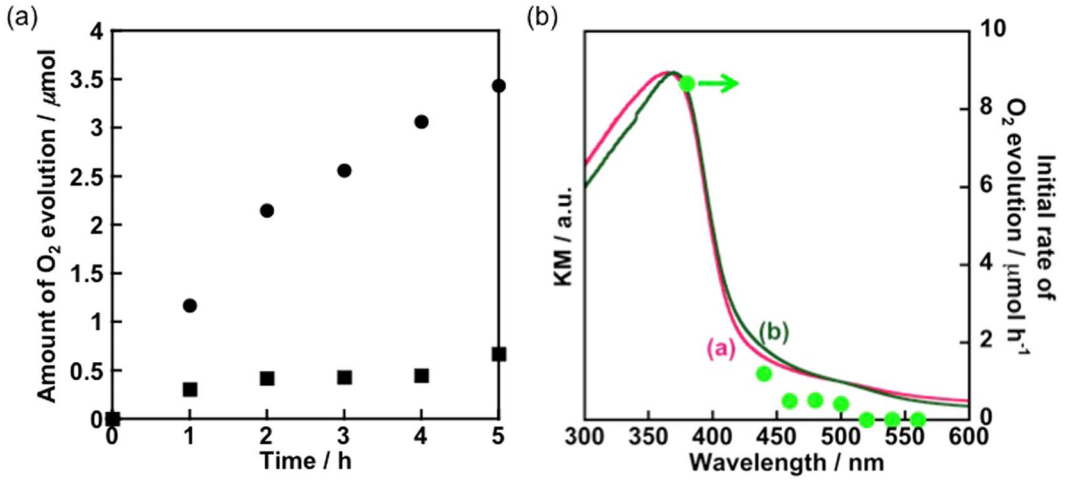

Figure 5. (**a**) Heterogeneous O_2 evolution reactions over Nb_2O_5-NW(P) (black squares) and Nb_2O_5:Rh-NW(P) (black circles). Each sample weight is 0.3 g. A 0.01 mM aqueous $AgNO_3$ solution and visible light provided from a 300-W Xe lamp with a Y44 filter were used as the sources of the electron acceptor and light, respectively. Figure 5b shows the wavelength dependence of the O_2 evolution reaction (pale-green circles), together with the DRS spectra shown in Fig. 3.

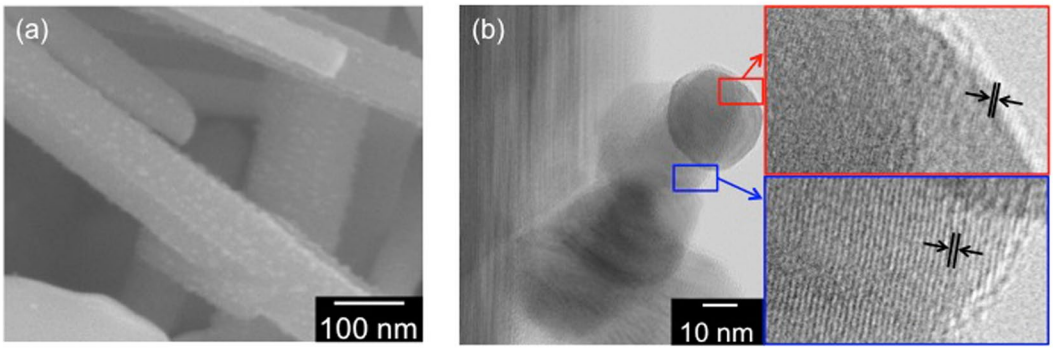

Figure 6. (**a**) FE-SEM image of Au/CdS/Nb_2O_5:Rh-NW(P) obtained from a short-term, rotating CVD process. (**b**) TEM images of Au/CdS/Nb_2O_5:Rh-NW(P). The calculated lattice spacings in the red and blue frames (2.1 and 3.1 Å) are in good agreement with the *d*-spacings of the (200) plane of Au ($d_{200} = 2.039$ Å) and of the (101) plane of CdS ($d_{101} = 3.164$ Å), respectively.

The wavelength dependence of the O_2 evolution reaction, shown in Fig. 5b, clearly shows that the absorption edge from Rh^{3+} correlates well with the onset wavelength for O_2 evolution. On the other hand, due to a lack of driving force for electron transfer from the conduction-band minimum of the host for water reduction (as shown in the band structure in Fig. 3), Nb_2O_5:Rh-NW(P) shows negligible photoresponse for H_2 evolution, even with fine Pt particles deposited by a unique, intermittent irradiation of visible light (Figures S6 and S7).

Investigating a heterostructure for efficient charge transfer. The combination of the metal oxide and sulphide is well suited to perform water splitting, as reported in recent studies[21–31, 40, 41]. Ideally, an H_2-evolving sulphide, such as CdS, is placed on the reduction site of the O_2-evolving oxide; however, the strategy is poorly known. The VLS mechanism, guided by a metal catalyst, has been extensively used for the controlled growth of nanomaterials. However, in general, the low permeability of the reactive gas into the powder hinders the reaction of the gaseous sulphide and Au on Nb_2O_5:Rh-NW(P). Therefore, a CVD reaction was carried out using mechanical rotation to help expose the unreacted powder to the gaseous sulphide[34].

First, a Au nanocatalyst for the VLS mechanism was photochemically deposited on the reduction sites of Nb_2O_5:Rh-NW(P) in the presence of an electron donor [Au/Nb_2O_5:Rh-NW(P)][19]. The existence of Au, with an undetectable size at the sensitivity of FE-SEM, on Nb_2O_5:Rh-NW(P) was confirmed from the Au 4f XPS spectrum (Figure S8). Upon prolonged a rotating CVD process with CdS, the nanostructure undergoes a change in shape to branched nanowires (Figure S9). Each branch possesses particulate tip, evidencing that the VLS mechanism occurred on the nanowire. The Raman spectra reveal the growth of peaks corresponding to CdS, indicating that the branches are composed of CdS (Figure S10). Considering the carrier-transfer distance, a shorter branch should be favourable for electron transfer across the oxide-sulphide interface. Figure 6a shows an FE-SEM image

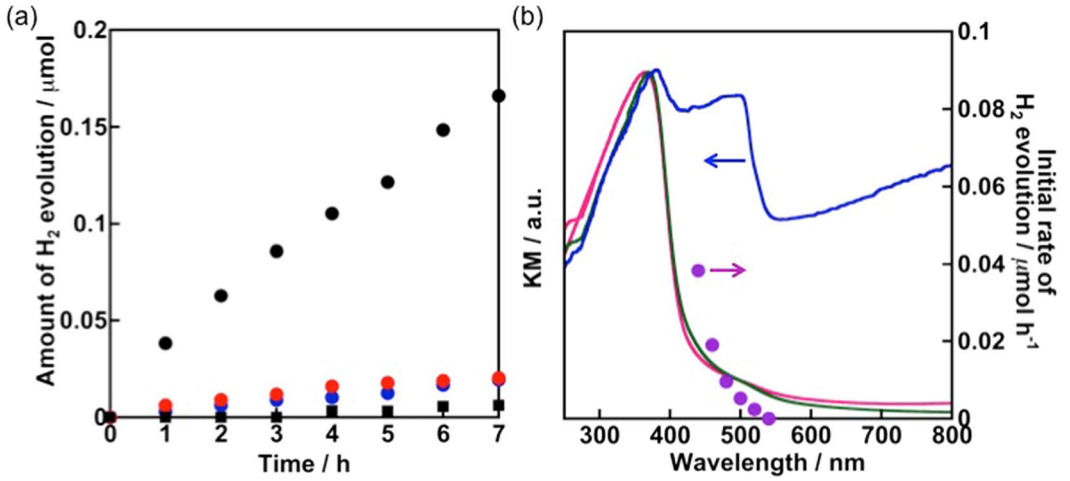

Figure 7. (**a**) Heterogeneous H_2 evolution over Au/CdS/Nb_2O_5:Rh-NW(P) (black circles), Nb_2O_5:Rh-NW(P) with randomly deposited CdS (red circles), CdS (blue circles), and Au/Nb_2O_5:Rh-NW (P) (black squares). Each sample weight is 0.1 g, except for CdS (0.31 mg). A 10 vol% aqueous methanol solution and visible light provided from a 300-W Xe lamp with a Y44 filter were used as the sources of the electron donor and light, respectively. Figure 7b shows the wavelength dependence for H_2 evolution over Au/CdS/Nb_2O_5:Rh-NW(P) (purple circles), together with the DRS of Au/CdS/Nb_2O_5:Rh-NW(P) (blue line) and Nb_2O_5:Rh-NW(P) (red and green lines, as shown in Fig. 3).

indicating that a short-term, rotating CVD process results in highly dispersed nanoparticles with an average size of 17 nm throughout the nanowires [Au/CdS/Nb_2O_5:Rh-NW(P)]. Additionally, TEM images show the existence of CdS with a Au tip on a nanowire (Fig. 6b).

Under irradiation of visible light ($\lambda > 440$ nm) in a 10 vol% methanol solution, Au/CdS/Nb_2O_5:Rh-NW(P) achieves an order of magnitude higher performance for H_2 evolution than the following standards: Pt/Nb_2O_5:Rh-NW(P), Au/Nb_2O_5:Rh-NW(P), an equivalent amount of CdS contained in Au/CdS/Nb_2O_5:Rh-NW(P), and Nb_2O_5:Rh-NW(P) with randomly deposited CdS (Fig. 7a). In addition, the wavelength dependence, shown in Fig. 7b, clearly indicates that CdS loaded onto the nanowires does not perform well by itself (shown with the blue circles in Fig. 7a) at 520 nm, corresponding to the absorption by only CdS. When a shorter wavelength is utilizing corresponding to the absorption edge of Nb_2O_5:Rh-NW, a steep increase in H_2 evolution activity is observed. Therefore, the observed photocatalytic H_2 evolution over Au/CdS/Nb_2O_5:Rh-NW(P) is driven by electron transfer from two-photon excitation. The rate of H_2 evolution decreased during 11.5 h of photocatalytic reaction (Figure S11a); however, the elution of CdS was not seen in ICP experiments. On the other hand, the nanowire structures were found to partially decompose possibly by stirring in a reaction cell, which can be sometimes seen with other nanowire system (Figure S11b). Au is frequently used as a cocatalyst for H_2 evolution and as a photosensitizer to harness its surface plasmon resonance[42,43]. In this work, the loaded Au provided a modest effect on H_2 evolution over Nb_2O_5:Rh-NW(P) (Fig. 7a). The degree of improvement will be not significant, even over CdS, particularly considering previous research[44].

In the light of these results, a plausible primary reaction mechanism is shown in Fig. 8. Following visible-light capture, an electron-hole pair is generated in both Nb_2O_5:Rh-NW and CdS. The hole in the Rh^{3+} impurity level is consumed by methanol, and the electron in the conduction band of CdS reduces water to form H_2. In addition to methanol[45], the conduction-band electron in Nb_2O_5:Rh-NW promptly merges with the valence-band hole in CdS due to a larger driving force for electron transfer than the driving force for water reduction. If electron transfer follows the heterojunction[46], photogenerated electrons accumulate on the conduction band of Nb_2O_5:Rh-NW, and holes accumulate on the valence band of CdS. In that case, the photocatalyst composite will show no photoresponse, as with bare Nb_2O_5:Rh-NW(P), because Au is located on top of CdS. However, H_2 evolution was highly improved, indicating that H_2 is evolved over CdS rather than Nb_2O_5:Rh-NW. Furthermore, hole accumulation should facilitate photocorrosion of CdS; however, such a phenomenon was not observed. Thus, we conclude that electron transfer mainly follows a Z-scheme. The vast improvement originates from CdS directly linking to the reduction site of Nb_2O_5:Rh-NW and hence efficient electron transfer across the oxide-sulphide nanointerface occurs.

Conclusions

Self-catalytic growth and MOCVD were combined in a single synthesis approach to form Nb_2O_5:Rh-NW with two different macroscopic morphologies. Rh was doped into the Nb_2O_5 lattice, forming mixed-valence Rh^{3+} and Rh^{4+} states. The free-standing nanowire film functioned as a photoanode for photoelectrochemical water splitting under visible-light irradiation ($\lambda > 440$ nm). The powder was found to oxidize water in the presence of an electron acceptor. To boost the H_2-evolution performance, Au was photodeposited on the reduction site of Nb_2O_5:Rh-NW, and using a rotating CVD apparatus, CdS was directly bonded to the reduction site through a VLS mechanism.

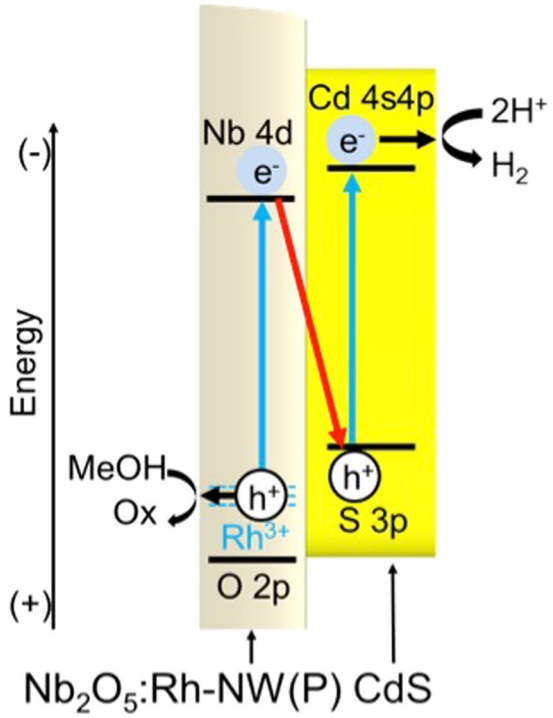

Figure 8. Plausible primary electron-transfer mechanism occurring on Au/CdS/Nb_2O_5:Rh-NW(P).

The 3D heteronanostructure consisting of Nb_2O_5:Rh-NW stems with short Au/CdS branches showed largely improved H_2-evolution performance due to efficient carrier transfer at the oxide-sulphide nanointerface.

Methods

0.1 and 0.25 mm-thick Nb foils (99.9%) were purchased from the Nilaco Corporation. Rh(acac)$(CO)_2$ (acac = acetylacetonato, 39.9% as Rh, Tanaka Kikinzoku Kogyo) was employed as Rh source in the MOCVD process. CdS was purchased from Aldrich (99.995%). About other chemical substances we used those of high-grade qualities.

Nb_2O_5 nanowire fabrication with and without Rh doping. The film materials, Nb_2O_5-NW(F) and Nb_2O_5:Rh-NW(F), and the powdered forms, Nb_2O_5-NW(P) and Nb_2O_5:Rh-NW(P), were synthesized from 0.1- and 0.25-mm-thick Nb foils, respectively. Prior to the synthesis, Nb foil with dimensions of 1 cm × 2 cm was rinsed with water and then ethanol three times under sonication for 3 min. The foil was finally rinsed in acetone and dried under a N_2 flow. The clean foil was placed at the centre of a quartz tube reactor [inner diameter (i.d.) = 1.6 cm] equipped with an electric furnace with a length of 14 cm. The following modified Varghese's method was used to obtain the non-doped nanowires, Nb_2O_5-NW(F) and Nb_2O_5-NW(P)[37]. After the pressure in the quartz tube reached ~15 Pa, the sample tube was heated to 1173 K with a ramping rate of 318 K min^{-1} while flowing 100-sccm Ar through an 1/8-inch stainless steel tubing (reaching a total pressure of ~1.2×10^3 Pa). O_2 (400 sccm) was introduced through the same-sized tubing for 1.5 h. Rh-doped nanowires, Nb_2O_5:Rh-NW(F) and Nb_2O_5:Rh-NW(P) were grown under the same conditions, with the exception that Ar containing Rh(acac)$(CO)_2$, vaporized at 343 K, and O_2 were utilized at the same time.

Fabrication of the Rh-doped Nb_2O_5 nanowires with CdS. Using a photodeposition method, a Au catalyst was loaded on reduction sites of Nb_2O_5:Rh-NW(P) (Au/Nb_2O_5:Rh-NW). Nb_2O_5:Rh-NW(P) was mixed in a 10 vol% aqueous methanol solution of $HAuCl_3$ (42 μmol L^{-1}), and the suspension stirred at 400 rpm was subjected to 20 cycles of a 10-s irradiation of visible light ($\lambda > 440$ nm). The intermittent irradiation allowed the Au catalyst to deposit with a tiny size, as observed in Figure S8. We used a home-built CVD apparatus with a double-walled quartz tube, inside of which housed two different powders, rotating independently by a rotary manipulator (ARIOS, RFT34S) and possessing a hole leading towards external evacuation [i.d.s of the inner and outer tubes were 1.6 and 0.5 cm, respectively]. CdS and Au/Nb_2O_5:Rh-NW were placed at the centre and at the downstream end of the furnace, respectively. After evacuation (~15 Pa), the quartz tube was heated to 1073 K for 40 min while flowing 25-sccm Ar and rotating at a speed of 30 rpm, resulting in the formation of CdS/Au/Nb_2O_5:Rh-NW. As a reference material, CdS [0.31 mg, equivalent to the amount of CdS contained in Au/CdS/Nb_2O_5:Rh-NW(P)] was randomly deposited on top of Nb_2O_5:Rh-NW(P) (100 mg) by an impregnation method. The CdS loading was evaluated by processing CdS/Au/Nb_2O_5:Rh-NW in HCl and analysing the eluent by ICP-AES.

Photocatalytic experiments. A standard three-electrode measurement combining the working electrode, a Pt coil counter electrode, and an Ag/AgCl (SSCE) reference electrode was carried out in a 0.1 M phosphate

buffer solution to assess the photoelectrochemical performance. A 100-W Xe lamp (USIO, UXL-500SX) with a Y44 filter was used as the light source. Heterogeneous H_2 and O_2 evolution reactions were examined using a gas-closed circulation system equipped with GC (Shimadzu, GC-8A). The photocatalyst was dispersed in a stirred aqueous solution (120 mL, 400 rpm), containing an electron donor (methanol) or an acceptor ($AgNO_3$), and was irradiated with visible light from 300 W Xe-lamp (CERMAX®, PE300BF) with a Y44 cut-off filter. For the experiments regarding wavelength dependence, incident-light-wavelengths were controlled by varying cut-off filters.

Material characterizations. Followings are the facilities used for characterizations of materials obtained. XRD (Rigaku MiniFlex600, Cu $K\alpha$), FE-SEM (JEOL JSM-6500F), DRS (JASCO V-670), Raman (Horiba LabRAM HR-800, excitation wavelength of 532 nm), XPS (JEOL JPS-9000, Mg Kα as an X-ray source), and ICP-AES (Seiko Instrument Inc. SPS1500).

Data availability. All data are included in this published article (and its Supplementary Information files).

References

1. Maeda, K. Z-scheme water splitting using two different semiconductor photocatalysts. *ACS Catal.* **3**, 1486–1503 (2013).
2. Zhou, P., Yu, J. & Jaroniec, M. All-solid-state Z-scheme photocatalytic systems. *Adv. Mater.* **26**, 4920–4935 (2014).
3. White, J. L. *et al*. Light-driven heterogeneous reduction of carbon dioxide: photocatalysts and photoelectrodes. *Chem. Rev.* **115**, 12888–12935 (2015).
4. Cheng, C. & Fan, H. J. Branched nanowires: synthesis and energy applications. *Nano Today* **7**, 327–343 (2012).
5. Osterloh, F. E. Inorganic nanostructures for photoelectrochemical and photocatalytic water splitting. *Chem. Soc. Rev.* **42**, 2294–2320 (2013).
6. Liu, C., Dasgupta, N. P. & Yang, P. Semiconductor nanowire for artificial photosynthesis. *Chem. Mater.* **26**, 415–422 (2014).
7. Wang, G. *et al*. Hydrogen-treated TiO_2 nanowire arrays for photoelectrochemical water splitting. *Nano Lett.* **11**, 3026–3033 (2011).
8. Bai, J. *et al*. A novel 3D ZnO/Cu_2O nanowire photocathode material with highly efficient photoelectrocatalytic performance. *J. Mater. Chem. A* **3**, 22996–23002 (2015).
9. Li, Y. & Chen, H. Facile fire treatment of nanostructured hematite with an enhanced photoelectrochemical water splitting performance. *J. Mater. Chem. A* **4**, 14974–14977 (2016).
10. Hong, T., Liu, Z., Zheng, X., Zhang, J. & Yan, L. Efficient photoelectrochemical water splitting over Co_3O_4 and Co_3O_4/Ag composite structure. *Appl. Catal. B* **202**, 454–459 (2017).
11. Hwang, Y. J., Wu, C. H., Hahn, C., Jeong, E. & Yang, P. Si/InGaN core/shell hierarchical nanowire arrays and their photoelectrochemical properties. *Nano Lett.* **12**, 1678–1682 (2012).
12. Sheng, W. *et al*. Quantum dot-sensitized hierarchical micro/nanowire architecture for photoelectrochemical water splitting. *ACS Nano* **8**, 7163–7169 (2014).
13. Ebaid, M., Kang, J.-H. & Ryu, S.-W. Controllable synthesis of vapor-liquid-solid grown GaN nanowires for photoelectrochemical water splitting applications. *J. Electrochem. Soc.* **162**, H264–H270 (2015).
14. Kornienko, N. *et al*. Growth and photoelectrochemical energy conversion of wurtzite indium phosphide nanowire arrays. *ACS Nano* **10**, 5525–5535 (2016).
15. Huang, H. *et al*. Structure inherited synthesis of N-doped highly ordered mesoporous Nb_2O_5 as robust catalysts for improved visible light photoactivity. *Nanoscale* **6**, 7274–7280 (2014).
16. Hong, Y. *et al*. Efficient and stable Nb_2O_5 modified g-C_3N_4 photocatalyst for removal of antibiotic pollutant. *Chem. Eng. J.* **299**, 74–84 (2016).
17. Yue, Z. *et al*. A novel heterogeneous hybrid by incorporation of Nb_2O_5 microspheres and reduced graphene oxide for photocatalytic H_2 evolution under visible light irradiation. *RSC Adv.* **5**, 47117–47124 (2015).
18. Yue, Z. *et al*. Noble-metal-free hetero-structural CdS/Nb_2O_5/N-doped-grapheneternary photocatalytic system as visible-light-driven photocatalyst for hydrogen evolution. *Appl. Catal. B* **201**, 202–210 (2017).
19. Saito, K. & Kudo, A. Diameter-dependent photocatalytic performance of niobium pentoxide nanowires. *Dalton Trans.* **42**, 6867–6872 (2013).
20. Kudo, A. & Miseki, Y. Heterogeneous photocatalyst materials for water splitting. *Chem. Soc. Rev.* **38**, 253–278 (2009).
21. Zhang, L. J., Li, S., Liu, B. K., Wang, D. J. & Xie, T. F. Highly efficient CdS/WO_3 photocatalysts: Z-scheme photocatalytic mechanism for their enhanced photocatalytic H_2 evolution under visible light. *ACS Catal.* **4**, 3724–3729 (2014).
22. Yu, S., Lee, S. Y., Yeo, J., Han, J. W. & Yi, J. Kinetic and mechanistic insights into the all-solid-state Z-schematic system. *J. Phys. Chem. C* **118**, 29583–29590 (2014).
23. Iwashina, K., Iwase, A., Ng, Y. H., Amal, R. & Kudo, A. Z-schematic water splitting into H_2 and O_2 using metal Sulfide as a hydrogen-evolving photocatalyst and reduced graphene oxide as a solid-state electron mediator. *J. Am. Chem. Soc.* **137**, 604–607 (2015).
24. Li, W. *et al*. Fabrication of sulfur-doped g-C_3N_4/Au/CdS Z-scheme photocatalyst to improve the photocatalytic performance under visible light. *Appl. Catal. B* **168–169**, 465–471 (2015).
25. Ma, K., Yehezkeli, O., Domaille, D. W., Funke, H. H. & Cha, J. N. Enhanced hydrogen production from DNA-assembled Z-scheme TiO_2–CdS photocatalyst systems. *Angew. Chem. Int. Ed.* **127**, 11652–11656 (2015).
26. Jin, J., Yu, J., Guo, D., Cui, C. & Ho, W. A hierarchical Z-scheme CdS–WO_3 photocatalyst with enhanced CO_2 reduction activity. *Small* **11**, 5262–5271 (2015).
27. Iwase, A. *et al*. Water splitting and CO_2 reduction under visible light irradiation using Z-scheme systems consisting of metal sulfides, CoO_x-loaded $BiVO_4$, and a reduced graphene oxide electron mediator. *J. Am. Chem. Soc.* **138**, 10260–10264 (2016).
28. Jia, X. *et al*. Direct Z-scheme composite of CdS and oxygen-defected $CdWO_4$: an efficient visible-light-driven photocatalyst for hydrogen evolution. *Appl. Catal. B* **198**, 154–161 (2016).
29. Li, S., Zhao, Q., Wang, D. & Xie, T. Work function engineering derived all-solid-state Z-scheme semiconductor-metal-semiconductor system towards high-efficiency photocatalytic H_2 evolution. *RSC Adv.* **6**, 66783–66787 (2016).
30. Zhou, F. Q., Fan, J. C., Xu, Q. J. & Min, Y. L. $BiVO_4$ nanowires decorated with CdS nanoparticles as Z-schemephotocatalyst with enhanced H_2 generation. *Appl. Catal. B* **201**, 77–83 (2017).
31. Guo, H.-L. *et al*. Artificial photosynthetic Z-scheme photocatalyst for hydrogen evolution with high quantum efficiency. *J. Phys. Chem. C* **121**, 107–114 (2017).
32. Wacaser, B. A. *et al*. Preferential interface nucleation: an expansion of the VLS growth mechanism for nanowires. *Adv. Mater.* **21**, 153–165 (2009).
33. Schmidt, V., Wittemann, J. V., Senz, S. & Gösele, U. Silicon nanowires: a review on aspects of their growth and their electrical properties. *Adv. Mater.* **21**, 2681–2702 (2009).
34. Zhang, J., Tu, R. & Goto, T. Preparation of Ni-precipitated hBN powder by rotary chemical vapor deposition and its consolidation by spark plasma sintering. *J. Alloy Comp.* **502**, 371–375 (2010).
35. Suhonen, S. *et al*. Effect of Ce-Zr mixed oxides on the chemical state of Rh in alumina supported automotive exhaust catalysts studied by XPS and XRD. *Appl. Catal. A* **218**, 151–160 (2001).

36. Niishiro, R. *et al*. Photocatalytic O_2 evolution of rhodium and antimony-codoped rutile-type TiO_2 under visible light irradiation. *J. Phys. Chem. C* **111**, 17420–17426 (2007).
37. Niishiro, R., Tanaka, S. & Kudo, A. Hydrothermal-synthesized $SrTiO_3$ photocatalyst codoped with rhodium and antimony with visible-light response for sacrificial H_2 and O_2 evolution and application to overall water splitting. *Appl. Catal. B* **150–151**, 187–196 (2014).
38. Varghese, B., Haur, S. C. & Lim, C.-T. Nb_2O_5 nanowires as efficient electron field emitters. *J. Phys. Chem. C* **112**, 10008–10012 (2008).
39. Lv, Y., Yao, W., Zong, R. & Zhu, Y. Fabrication of wide-range-visible photocatalyst Bi_2WO_{6-x} nanoplates via surface oxygen vacancies. *Sci. Rep.* **6**, 1–9 (2016).
40. Luo, J. *et al*. Homogeneous photosensitization of complex TiO_2 nanostructures for efficient solar energy conversion. *Sci. Rep.* **2**, 1–6 (2012).
41. Luo, J. *et al*. TiO_2/(CdS, CdSe, CdSeS) nanorod heterostructures and photoelectrochemical properties. *J. Phys. Chem. C* **116**, 11956–11963 (2012).
42. Iwase, A., Kato, H. & Kudo, A. The effect of Au cocatalyst loaded on La-doped $NaTaO_3$ on photocatalytic water splitting and O_2 photoreduction. *Appl. Catal. B* **136–137**, 89–93 (2013).
43. Tanaka, A., Teramura, K., Hosokawa, S., Kominami, H. & Tanaka, T. Visible light-induced water splitting in an aqueous suspension of a plasmonic Au/TiO_2 photocatalyst with metal co-catalysts. *Chem. Sci* **8**, 2574–2580 (2017).
44. Zong, X. *et al*. Enhancement of photocatalytic H_2 evolution on CdS by loading MoS_2 as cocatalyst under visible light irradiation. *J. Am. Chem. Soc.* **130**, 7176–7177 (2008).
45. Ben-Shahar, Y. & Banin, U. Hybrid semiconductor-metal nanorods as photocatalysts. *Top. Curr. Chem.* **374**(54), 1–26 (2016).
46. Marschall, R. Semiconductor composites: strategies for enhancing charge carrier separation to improve photocatalytic activity. *Adv. Funct. Mater.* **24**, 2421–2440 (2014).

Acknowledgements

K.S. acknowledges financial supports from the Union Tool Scholarship Foundation, the Uchida Energy Science Promotion Foundation, the Iwatani Naoji Foundation, the Yashima Environmental Technology Foundation, and JSPS KAKENHI (Grant Number 16K04885).

Author Contributions

Building on the preliminary results from Y.S. and S.O., T.S., M.Y., and K.S. advanced the research and wrote the manuscript. T.Y. and M.Y. gave fruitful advice and reviewed the manuscript.

Additional Information

Supplementary information accompanies this paper at doi:10.1038/s41598-017-05292-2

Competing Interests: The authors declare that they have no competing interests.

Publisher's note: Springer Nature remains neutral with regard to jurisdictional claims in published maps and institutional affiliations.